Exchange and Quadrupole Broadening of Nuclear Acoustic Resonance Line Shapes in the III-V Semiconductors*

R. K. SUNDFORS
Arthur Holly Compton Laboratory of Physics, Washington University, Saint Louis, Missouri 63130
(Received 10 April 1969)

Nuclear acoustic resonance (NAR) and nuclear magnetic resonance (NMR) are used to study the linewidths, second moments, and line shapes of nuclear-spin systems of InAs, InSb, GaAs, GaSb, and AlSb. These cw measurements are made at frequencies of 8–10 MHz and at 300°K in single crystals with intrinsic or near intrinsic concentrations of impurities. Different NAR and NMR linewidths for the same nuclear-spin system are explained by the different interaction Hamiltonians for spin-phonon and spin-photon couplings to the nuclear-spin system. When the magnetic field is along ⟨001⟩ directions, the resonance line shapes are broadened by dipole-dipole and isotropic nuclear-exchange interactions. When the magnetic field is rotated from ⟨001⟩ directions, increased broadening of the resonance line shapes is explained by small anisotropic dipole-dipole and much larger anisotropic quadrupole interactions. The measured like-spin and unlike-spin exchange constants agree with an exchange-constant dependence on the inverse fourth power of the internuclear distance. Like-spin and unlike-spin exchange constants are determined at the nuclear positions in each compound and used with a theory for indirect nuclear-spin exchange to predict the *s*-character electronic wave-function density. The strongly anisotropic quadrupole broadening is explained by electric field gradients produced by the electric fields associated with ionized substitutional impurities. From the measured field gradients, antishielding constants at the In, Sb, Ga, and As nuclear positions are determined relative to each other.

I. INTRODUCTION

NUCLEAR magnetic resonance (NMR) linewidth and line-shape studies have given a wealth of information about the interactions between a nucleus and its environment. In particular, NMR techniques have been applied to analyze the resonance line broadening mechanisms in the $A^{III}B^{V}$ compounds. For low concentrations of impurities in these compounds, broadening of NMR linewidths beyond calculated dipole-dipole widths has been explained[1,2] as due to nuclear exchange between unlike-spin systems. This nuclear-exchange interaction involves an indirect nuclear-spin coupling[3,4] via the hyperfine interaction between electronic and nuclear spins. The theory of Anderson[1,5] for indirect exchange in semiconductors has been used with the experimental linewidths in order to estimate[1,2] the product of the *s* character part of the electronic wave-function densities at the A and B nuclear positions.

For large concentrations of substitutional impurities, additional broadening of the NMR line shapes in the $A^{II}B^{V}$ compounds has been explained[6–8] as due to quadrupole broadening from electric field gradients associated with the substitutional impurities. Neutral, donor, and acceptor impurities have produced quadrupole broadening for an estimated 10^3 nuclei surrounding an impurity. In order to explain on the basis of a continuum model the effects of the field gradients associated with the ionized donor and acceptor impurities, it has been necessary to introduce antishielding factors[9] of 10^3 for $In^{115}Sb$.

Nuclear-spin acoustic-phonon resonant coupling can be used to study and to characterize in much more detail exchange and quadrupole broadening processes in the $A^{III}B^{V}$ compounds. Because of the difference of the spin-phonon and spin-photon perturbation of the nuclear-spin system, the resonance line shapes and linewidths may differ depending on whether a spin-phonon or spin-photon experiment is used. Loudon[10] has computed the spin-phonon second and fourth moments in the case of like spins for dipole-dipole and exchange interactions. Koloskova and Kopvillem[11,12] have used the method of Kubo and Tomita[13] to compute the second and fourth moments also in the case of like spins for dipole-dipole, exchange, and a specific quadrupole interaction. The work of Van Vleck[14] gives the spin-photon second and fourth moments in the case of like- and unlike-spin systems for dipole-dipole and exchange interactions. Finally, Bersohn[15] gives second-moment expressions for spin-photon quadrupole broadening.

In the $A^{III}B^{V}$ compounds, nuclear-spin acoustic-phonon coupling occurs via the dynamic electric

* Work sponsored by the National Science Foundation under NSF Grant No. 9278.

[1] R. G. Shulman, J. M. Mays, and D. W. McCall, Phys. Rev. **100**, 692 (1955).
[2] R. G. Shulman, B. J. Wyluda, and H. R. Hrostowski, Phys. Rev. **109**, 808 (1958).
[3] M. A. Ruderman and C. Kittel, Phys. Rev. **96**, 99 (1954).
[4] N. Bloembergen and T. J. Rowland, Phys. Rev. **97**, 1679 (1955).
[5] P. W. Anderson, Phys. Rev. **99**, 623 (1955).
[6] E. H. Rhoderick, Phil. Mag. **3**, 545 (1958).
[7] E. H. Rhoderick, J. Phys. Chem. Solids **8**, 498 (1958).
[8] D. J. Oliver, J. Phys. Chem. Solids **11**, 257 (1959).
[9] R. M. Sternheimer, Phys. Rev. **146**, 140 (1966).
[10] R. Loudon, Phys. Rev. **119**, 919 (1960).
[11] N. G. Koloskova and U. Kh. Kopvillem, Zh. Eksperim i. Teor. Fiz. **38**, 1351 (1960) [English transl.: Soviet Phys.—JETP **11**, 973 (1960)].
[12] N. G. Koloskova and U. Kh. Kopvillem, Fiz. Tverd. Tela. **4**, 697 (1962) [English transl.: Soviet Phys.—Solid State **4**, 508 (1963)].
[13] R. Kubo and K. Tomita, J. Phys. Soc. Japan **9**, 888 (1954).
[14] J. H. Van Vleck, Phys. Rev. **74**, 1168 (1948).
[15] R. Bersohn, J. Chem. Phys. **20**, 1505 (1952).

quadrupole interaction.[16] We call the cw resonance experiment, which measures the ultrasonic attenuation due to absorption of elastic strain energy by the nuclear-spin system, nuclear acoustic resonance[17] (NAR).

In this paper we report the experimental measurements of the NAR and NMR line shapes and linewidths of the nuclear-spin systems in single crystals of InAs, InSb, GaAs, GaSb, and AlSb. We also discuss in detail the determination of the broadening mechanisms, the like-spin and unlike-spin exchange broadening, and the source of the quadrupole broadening.

In Sec. II, we consider the theory for the broadening of NAR line shapes. In Sec. III, the experimental linewidth and line-shape data are presented. In Sec. IV, we analyze the experimental data. In Sec. V, there is a brief summary of the important points developed in Secs. II and IV.

II. THEORY

We demonstrate in Sec. IV that NAR and NMR linewidths for nuclear-spin systems in $A^{III}B^{V}$ compounds can be explained as due to contributions from several different interactions. These are the anisotropic dipole-dipole interaction between like and unlike spins, the isotropic exchange interaction between like and unlike spins, and an anisotropic quadrupole interaction. We extend the second-moment calculations of other authors[10–12,15] to cover spin-phonon coupling for dipole-dipole and exchange interactions between unlike spins and for quadrupole interactions. The quadrupole interaction second moment is computed without reference to a specific model for field gradient generation.

We consider a system of N nuclear spins per unit volume in an external magnetic field H, which is directed along the z axis. We assume two different nuclear-spin systems, whose nuclei have spin angular momenta $\hbar\mathbf{I}$ and $\hbar\mathbf{S}$. The two nuclear-spin systems have resonances which do not overlap. The resonance experiment is performed with the nuclear spins I. It is further assumed that the separation between Zeeman levels is very large compared to the energy splittings produced by dipole-dipole, exchange, or quadrupole interactions. The energy splittings of these interactions have similar magnitudes.

Following the work of Van Vleck[14] and of Loudon[10], we calculate the second moment from the expression

$$\langle\hbar^2\omega^2\rangle_{\rm av}=-\mathrm{Tr}[\mathcal{H},\mathcal{G}]^2/\mathrm{Tr}[\mathcal{G}^2]. \tag{1}$$

The system Hamiltonian $\mathcal{H}$ is defined by

$$\mathcal{H}=\mathcal{H}_{0I}+\mathcal{H}_{0S}+\mathcal{H}_{DI}+\mathcal{H}_{DS}+\mathcal{H}_{DIS}+\mathcal{H}_{EI}+\mathcal{H}_{ES}+\mathcal{H}_{EIS}+\mathcal{H}_{Q}, \tag{2}$$

where $\mathcal{H}_{0I}$ is the Zeeman term for resonant spins I, $\mathcal{H}_{0S}$ is the Zeeman term for spins S, $\mathcal{H}_{DI}$ is the dipole-dipole term for like spins I, $\mathcal{H}_{DS}$ is the dipole-dipole term for like spins S, $\mathcal{H}_{DIS}$ is the dipole-dipole term for unlike spins I and S,

$$\mathcal{H}_{EI}=\sum_{j<k}A_{jk}\mathbf{I}_j\cdot\mathbf{I}_k, \tag{3a}$$

$$\mathcal{H}_{ES}=\sum_{j<k}\tilde{A}_{jk}'\mathbf{S}_j\cdot\mathbf{S}_k, \tag{3b}$$

$$\mathcal{H}_{EIS}=\sum_{j,k}\tilde{A}_{jk}\mathbf{I}_j\cdot\mathbf{S}_k, \tag{3c}$$

$$\mathcal{H}_{Q}=\sum_{j}\mathbf{E}_j[3I_{zj}^2-I_j(I_j+1)], \tag{3d}$$

A_{jk} is the exchange term for like spins I, $\tilde{A}_{jk}'$ is the exchange term for like spin S, $\tilde{A}_{jk}$ is the exchange term for unlike spins I and S, and

$$E_j=\frac{eQ}{4I(2I-1)}\left(\frac{\partial^2V}{\partial z^2}\right)_j=AV_{zzj}. \tag{4}$$

The interaction Hamiltonian for nuclear-spin-phonon coupling $\mathcal{G}$ can be written[18]

$$\mathcal{G}=A\sum_j[(I_{+j}I_{zj}+I_{zj}I_{+j})V_{-1j}+(I_{-j}I_{zj}+I_{zj}I_{-j})V_{+1j}+I_{+j}^2V_{-2j}+I_{-j}^2V_{+2j}], \tag{5}$$

where

$$V_{\pm1}=V_{xy}\pm iV_{yz}, \tag{6a}$$

$$V_{\pm2}=\tfrac{1}{2}(V_{xx}-V_{yy})\pm iV_{xy}. \tag{6b}$$

It is evident that the spin-phonon interaction Hamiltonian is bilinear in the spin operators and differs from the interaction Hamiltonian for NMR,

$$\mathcal{G}'\propto\sum_j I_{xj}.$$

NAR transitions of interest are centered at the frequencies $\omega_1=\gamma_I H$ and $\omega_2=2\gamma_I H$. If m is defined as the magnetic quantum number labeling the orientation of nuclear spin I, then ω_1 corresponds to $\Delta m=\pm1$ transitions and ω_2 to $\Delta m=\pm2$ transitions. To simplify future expressions, we define NAR 1 and NAR 2 to be spin-phonon resonances for $\Delta m=\pm1$ and $\Delta m=\pm2$ transitions, respectively.

The second moments for the computed resonance lines of NAR 1 and NAR 2 are given in Eqs. (7) and (8):

$$\begin{aligned}\langle\hbar^2\Delta\omega^2\rangle_{\rm av\ NAR\ 1}&=2I(I+1)\sum_j A_{jk}^2+2I(I+1)\sum_j A_{jk}B_{jk}\\&+3I(I+1)\sum_j B_{jk}^2+\tfrac{1}{3}S(S+1)\sum_j\tilde{A}_{jk}^2\\&-\tfrac{4}{3}S(S+1)\sum_j\tilde{A}_{jk}\tilde{B}_{jk}+\tfrac{4}{3}S(S+1)\sum_j\tilde{B}_{jk}^2\\&+(9/7)[12I(I+1)-17]N^{-1}\sum_j E_j^2,\end{aligned} \tag{7}$$

[16] R. K. Sundfors, Phys. Rev. **177**, 1221 (1969). In this reference, the theoretical ratio of the ionic part of $(S_{11}-S_{12})/S_{44}$ should be -3.0.

[17] D. I. Bolef, *Physical Acoustics* (Academic Press Inc., New York, 1966), Vol. 4A, Chap. 3.

[18] M. H. Cohen and F. Reif, *Solid State Physics* (Academic Press Inc., New York, 1957), Vol. 5, p. 322.

$$\langle\hbar^2\Delta\omega^2\rangle_{\text{av NAR 2}} = 2I(I+1)\sum_j A_{jk}^2 - 4I(I+1)\sum_j A_{jk}B_{jk} + 6I(I+1)\sum_j B_{jk}^2 + \tfrac{4}{3}S(S+1)\sum_j \tilde{A}_{jk}^2 - (16/3)S(S+1)\sum_j \tilde{A}_{jk}\tilde{B}_{jk} + (16/3)S(S+1)\sum_j \tilde{B}_{jk}^2 + (144/7)[I(I+1)-2]N^{-1}\sum_j \mathbf{E}_j^2, \quad (8)$$

where

$$B_{jk} = \gamma_I^2\hbar^2 r_{jk}^{-3}(\tfrac{3}{2}\cos^2\theta_{jk} - \tfrac{1}{2}), \quad (9a)$$

$$\tilde{B}_{jk} = \gamma_I\gamma_S\hbar^2 r_{jk}^{-3}(\tfrac{3}{2}\cos^2\theta_{jk} - \tfrac{1}{2}), \quad (9b)$$

θ_{jk} is the angle between the z axis, and $\mathbf{r}_{jk}$ is the vector from the j to k nucleus. In Eqs. (7) and (8), the like-spin dipole-dipole and exchange second moments agree with the results of Loudon.[10] The quadrupole second moments differ in form from the results of Koloskova and Kopvillem,[12] who use a particular model for the source of the electric field gradients. For a comparison between NAR and NMR second moments, we write in Eq. (10) the second moment for the spin-photon resonance centered at ω_1 and calculated by Bersohn[15] and Van Vleck[14]:

$$\langle\hbar^2\Delta\omega^2\rangle_{\text{av NMR}} = 3I(I+1)\sum_j B_{jk}^2 + \tfrac{1}{3}S(S+1)\sum_j \tilde{A}_{jk}^2 + \tfrac{4}{3}S(S+1)\sum_j \tilde{A}_{jk}\tilde{B}_{jk} + \tfrac{4}{3}S(S+1)\sum_j \tilde{B}_{jk}^2 + (9/5)[4I(I+1)-3]N^{-1}\sum_j E_j^2. \quad (10)$$

We now list a series of comparisons of properties of the second moments given in Eqs. (7), (8), and (10) for resonance lines observed at the *same* frequency. In these comparisons, we neglect the cross terms containing $A_{jk}B_{jk}$ and $\tilde{A}_{jk}\tilde{B}_{jk}$. Such cross terms will be shown in Sec. IV to be small in the $A^{\text{III}}B^{\text{V}}$ compounds.

(a) Dipole-dipole second moments for NMR and NAR 1 are identical.

(b) The ratio of NAR 1 and NAR 2 second moments for dipole-dipole interactions is two for like spins and one for unlike spins.

(c) Exchange second moments for NMR are nonzero only for the case of unlike-spin coupling.

(d) Exchange second moments for NAR are nonzero for both like- and unlike-spin coupling.

(e) The ratio of NAR 1 and NAR 2 second moments for exchange interactions is four for like spins and one for unlike spins.

(f) The quadrupole second moments for NAR and NMR obey the following inequality: NAR 1>NAR 2 >NMR.

A. Dipole-Dipole Contributions

The dipole-dipole second moments involving B_{jk}^2 and $\tilde{B}_{jk}^2$ in Eqs. (7), (8), and (10) can be calculated for the zinc-blende lattice characteristic of the $A^{\text{III}}B^{\text{V}}$ compounds. We make use of the definitions introduced by Van Vleck[14] for a crystal with cubic symmetry and write

$$\sum_j B_{jk}^2 = \tfrac{1}{8}[a + b(\lambda_1^4+\lambda_2^4+\lambda_3^4)]. \quad (11)$$

In Eq. (11), λ_1, λ_2, and λ_3 are the direction cosines of the applied magnetic field relative to the principal cubic axes. The constants a and b have the values

$$a = \sum_j r_{jk}^{-6}[7 - 9(\mu_{jk}^4+\nu_{jk}^4+\xi_{jk}^4)], \quad (12a)$$

$$b = \sum_j r_{jk}^{-6}[-9 + 15(\mu_{jk}^4+\nu_{jk}^4+\xi_{jk}^4)], \quad (12b)$$

where μ_{jk}, ν_{jk}, and ξ_{jk} are the direction cosines of $\mathbf{r}_{jk}$ relative to the principal cubic axes. We compute for the resonant nuclear-spin system on the fcc lattice of the zinc-blende structure that $a = 256\ a_0^{-6}$ and $b = -118\ a_0^{-6}$, where a_0 is the lattice constant. For the other lattice points, we compute $a' = 2491\ a_0^{-6}$ and $b' = -2390\ a_0^{-6}$. These values are found by determining the lattice sums out to the 25th shell and integrating from the 25th shell to infinity. An independent calculation[19] of a and b for the fcc lattice gives $a = 256\ a_0^{-6}$ and $b = -120\ a_0^{-6}$.

B. Exchange Broadening

Exchange broadening due to indirect exchange coupling between unlike nuclear spins has been used to explain NMR linewidths in InAs, InSb, GaAs, and GaSb.[1,2] Anderson[1,5] has proposed that isotropic indirect nuclear-spin exchange in semiconductors takes place via nondegenerate electrons of s character with high-momentum states. The dominant term for this exchange can be written for either like or unlike exchange as

$$A_{jk} = (8/9\pi)\gamma_e^2\gamma_j\gamma_k\hbar^2\Omega^2\zeta_j\zeta_k\Psi_j^2(0)\Psi_k^2(0)m^* r_{jk}^{-4}, \quad (13)$$

where Ω is the atomic volume,

$$\zeta_j = [\Psi_j(0)_{\text{hole}}{}^*\Psi_j(0)_{\text{electron}}]_{\text{solid}}/[\Psi_j^2(0)]_{\text{atom}},$$

$\Psi_j^2(0)$ is probability of finding outer s electrons of atom j at the nucleus,

$$m^* = 4(m_e^*)^{3/2}(m_h^*)^{3/2}(m_e^*+m_h^*)^{-2},$$

and m_e^* and m_h^* are the electron and hole effective masses, respectively. Anderson's expression for the exchange constant differs principally from another calculation[4] for semiconductors, where low-momentum states of the electron predominate by not having a negative exponential dependence on r_{jk}.

C. Quadrupole Broadening

The NAR 1 line shapes in several of the $A^{\text{III}}B^{\text{V}}$ compounds show first-order quadrupole splittings. In order to analyze these line shapes, it is useful to have

[19] E. Andrew, K. Swanson, and B. Williams, Proc. Phys. Soc. (London) **77**, 36 (1961).

the theoretical first-order quadrupole energy splittings due to a uniform field gradient V_{zz} and the relative transition probabilities between the quadrupole split energy levels for NAR 1, NAR 2, and NMR. We consider only the high-field case, where the quadrupole energy splittings are small compared to the Zeeman levels. In this high-field limit, the nuclear energy levels can be written[18]

$$E_m = -m\gamma\hbar H + A[3m^2 - I(I+1)]V_{zz}. \quad (14)$$

The transition probability dependence on spin can be written[17] as $(2m\pm1)^2(I\pm m+1)(I\mp m)$ for NAR 1, $(I\mp m)(I\mp m-1)(I\pm m+1)(I\pm m+2)$ for NAR 2, and $(I\pm m+1)(I\mp m)$ for NMR. In Tables I–IV, we show the quadrupole splitting of the energy levels in units of frequency, $\Delta = AV_{zz}/\hbar$, for $I=\frac{3}{2}$, $\frac{5}{2}$, $\frac{7}{2}$, and $\frac{9}{2}$. In these tables, the resonance frequency for no quadrupole broadening is ω_0. We observe in Tables II–IV that the relative transition probabilities for NAR 1 are larger for quadrupole transitions between energy levels with larger $|m|$ values. On the other hand, NMR and NAR 2 transition probabilities are larger for transitions between energy levels with smaller $|m|$ values.

For a uniform field gradient at each nuclear position in the crystal, a particular transition between first-order quadrupole split energy levels will have a second moment determined by the linewidth broadening mechanisms present in the absence of the field gradients. Using the method of Kambe and Ollom,[20] we have computed the second moments for NAR 1 and NAR 2 transitions for the cases of like and unlike spins. Our results show no change in the second moment of any

TABLE I. High-field transition frequencies and transition probabilities in NMR and NAR for $I=\frac{3}{2}$.

NMR Trans.	Freq.[a]	Prob.	NAR 1 Freq.[a]	Prob.	NAR 2 Trans.	Freq.[a]	Prob.
$+\frac{1}{2}\leftrightarrow+\frac{3}{2}$	$\omega_0+6\Delta$	3	$\omega_0+6\Delta$	3	$-\frac{1}{2}\leftrightarrow+\frac{3}{2}$	$2\omega_0+6\Delta$	3
$-\frac{1}{2}\leftrightarrow+\frac{1}{2}$	ω_0	4					
$-\frac{3}{2}\leftrightarrow-\frac{1}{2}$	$\omega_0-6\Delta$	3	$\omega_0-6\Delta$	3	$-\frac{3}{2}\leftrightarrow+\frac{1}{2}$	$2\omega_0-6\Delta$	3

[a] These frequencies are incorrectly given in Ref. 17.

TABLE II. High-field transition frequencies and transition probabilities in NMR and NAR for $I=\frac{5}{2}$.

NMR Trans.	Freq.	Prob.	NAR 1 Freq.	Prob.	NAR 2 Trans.	Freq.	Prob.
$+\frac{3}{2}\leftrightarrow+\frac{5}{2}$	$\omega_0+12\Delta$	5	$\omega_0+12\Delta$	5	$+\frac{1}{2}\leftrightarrow+\frac{5}{2}$	$2\omega_0+18\Delta$	5
$+\frac{1}{2}\leftrightarrow+\frac{3}{2}$	$\omega_0+6\Delta$	8	$\omega_0+6\Delta$	2	$-\frac{1}{2}\leftrightarrow+\frac{3}{2}$	$2\omega_0+6\Delta$	9
$-\frac{1}{2}\leftrightarrow+\frac{1}{2}$	ω_0	9					
$-\frac{3}{2}\leftrightarrow-\frac{1}{2}$	$\omega_0-6\Delta$	8	$\omega_0-6\Delta$	2	$-\frac{3}{2}\leftrightarrow+\frac{1}{2}$	$2\omega_0-6\Delta$	9
$-\frac{5}{2}\leftrightarrow-\frac{3}{2}$	$\omega_0-12\Delta$	5	$\omega_0-12\Delta$	5	$-\frac{5}{2}\leftrightarrow-\frac{1}{2}$	$2\omega_0-18\Delta$	5

TABLE III. High-field transition frequencies and transition probabilities in NMR and NAR for $I=\frac{7}{2}$.

NMR Trans.	Freq.	Prob.	NAR 1 Freq.	Prob.	NAR 2 Trans.	Freq.	Prob.
$+\frac{5}{2}\leftrightarrow+\frac{7}{2}$	$\omega_0+18\Delta$	7	$\omega_0+18\Delta$	21	$+\frac{3}{2}\leftrightarrow+\frac{7}{2}$	$2\omega_0+30\Delta$	7
$+\frac{3}{2}\leftrightarrow+\frac{5}{2}$	$\omega_0+12\Delta$	12	$\omega_0+12\Delta$	16	$+\frac{1}{2}\leftrightarrow+\frac{5}{2}$	$2\omega_0+18\Delta$	15
$+\frac{1}{2}\leftrightarrow+\frac{3}{2}$	$\omega_0+6\Delta$	15	$\omega_0+6\Delta$	5	$-\frac{1}{2}\leftrightarrow+\frac{3}{2}$	$2\omega_0+6\Delta$	20
$-\frac{1}{2}\leftrightarrow+\frac{1}{2}$	ω_0	16					
$-\frac{3}{2}\leftrightarrow-\frac{1}{2}$	$\omega_0-6\Delta$	15	$\omega_0-6\Delta$	5	$-\frac{3}{2}\leftrightarrow+\frac{1}{2}$	$2\omega_0-6\Delta$	20
$-\frac{5}{2}\leftrightarrow-\frac{3}{2}$	$\omega_0-12\Delta$	12	$\omega_0-12\Delta$	16	$-\frac{5}{2}\leftrightarrow-\frac{1}{2}$	$2\omega_0-18\Delta$	15
$-\frac{7}{2}\leftrightarrow-\frac{5}{2}$	$\omega_0-18\Delta$	7	$\omega_0-18\Delta$	21	$-\frac{7}{2}\leftrightarrow-\frac{3}{2}$	$2\omega_0-30\Delta$	7

TABLE IV. High-field transition frequencies and transition probabilities in NMR and NAR for $I=\frac{9}{2}$.

NMR Trans.	Freq.	Prob.	NAR 1 Freq.	Prob.	NAR 2 Trans.	Freq.	Prob.
$+\frac{7}{2}\leftrightarrow+\frac{9}{2}$	$\omega_0+24\Delta$	9	$\omega_0+24\Delta$	12	$+\frac{5}{2}\leftrightarrow+\frac{9}{2}$	$2\omega_0+42\Delta$	6
$+\frac{5}{2}\leftrightarrow+\frac{7}{2}$	$\omega_0+18\Delta$	16	$\omega_0+18\Delta$	12	$+\frac{3}{2}\leftrightarrow+\frac{7}{2}$	$2\omega_0+30\Delta$	14
$+\frac{3}{2}\leftrightarrow+\frac{5}{2}$	$\omega_0+12\Delta$	21	$\omega_0+12\Delta$	7	$+\frac{1}{2}\leftrightarrow+\frac{5}{2}$	$2\omega_0+18\Delta$	21
$+\frac{1}{2}\leftrightarrow+\frac{3}{2}$	$\omega_0+6\Delta$	24	$\omega_0+6\Delta$	2	$-\frac{1}{2}\leftrightarrow+\frac{3}{2}$	$2\omega_0+6\Delta$	25
$-\frac{1}{2}\leftrightarrow+\frac{1}{2}$	ω_0	25					
$-\frac{3}{2}\leftrightarrow-\frac{1}{2}$	$\omega_0-6\Delta$	24	$\omega_0-6\Delta$	2	$-\frac{3}{2}\leftrightarrow+\frac{1}{2}$	$2\omega_0-6\Delta$	25
$-\frac{5}{2}\leftrightarrow-\frac{3}{2}$	$\omega_0-12\Delta$	21	$\omega_0-12\Delta$	7	$-\frac{5}{2}\leftrightarrow-\frac{1}{2}$	$2\omega_0-18\Delta$	21
$-\frac{7}{2}\leftrightarrow-\frac{5}{2}$	$\omega_0-18\Delta$	16	$\omega_0-18\Delta$	12	$-\frac{7}{2}\leftrightarrow-\frac{3}{2}$	$2\omega_0-30\Delta$	14
$-\frac{9}{2}\leftrightarrow-\frac{7}{2}$	$\omega_0-24\Delta$	9	$\omega_0-24\Delta$	12	$-\frac{9}{2}\leftrightarrow-\frac{5}{2}$	$2\omega_0-42\Delta$	6

[20] K. Kambe and J. K. Ollom, J. Phys. Soc. Japan **11**, 50 (1956).

TABLE V. Experimental $A^{III}B^{V}$ single-crystal samples with physical properties determined by the supplier.

Compound	Type	Dopant	Average carrier concentration (cm^{-3})	Average mobility (cm^2/V sec)	Average resistivity (ohm cm)	Etch pit density[a] (cm^{-2})
InAs[b]	N	intrinsic	1.4×10^{16}	18 000	0.024	1100
InSb[b](1)	N	intrinsic	1.8×10^{14}[c]	55 000[c]	0.070[c]	3000
InSb[b](2)	P	Ge	1.5×10^{16}[c]	4500[c]	0.112[c]	100
InSb[b](3)	N	Te	1.7×10^{17}[c]	55 000[c]	0.00080[c]	600
GaAs[b]	N	intrinsic	1.4×10^{16}	3800	0.012	1200
GaSb[b]	P	intrinsic	1.7×10^{17}	570	0.066	5000
AlSb[d]	P	intrinsic	1.8×10^{16}	265	1.27	...

[a] Etch pit count is on the A (111) face.
[b] Supplied by Monsanto Chemical Co.
[c] These values are determined at 78°K, the remainder at 300°K.
[d] Obtained from Bell and Howell Research Laboratories.

transition for unlike spins when compared with the second moments due to dipole-dipole and exchange interactions, given by Eq. (7) and (8). For the case of like nuclear spins, our results are given in Eqs. (15) and (16). For NAR 1,

$$\langle\hbar^2\Delta\omega^2\rangle_{\text{av } 1/2\leftrightarrow 3/2}=\frac{4[2I^2(I+1)^2-5I(I+1)+(61/8)]}{2(2I+1)}\sum_j C_{jk}^2+\tfrac{1}{3}I(I+1)\sum_j D_{jk}^2-\frac{(2I-1)(2I+3)}{2(2I+1)}\times\sum_j C_{jk}D_{jk}, \quad (15a)$$

$$\langle\hbar^2\Delta\omega^2\rangle_{\text{av } 3/2\leftrightarrow 5/2}=\frac{4[2I^2(I+1)^2-17I(I+1)+(421/8)]}{2(2I+1)}\sum_j C_{jk}^2+\tfrac{1}{3}I(I+1)\sum_j D_{jk}^2-\frac{(2I-3)(2I+5)}{2(2I+1)}\times\sum_j C_{jk}D_{jk}, \quad (15b)$$

$$\langle\hbar^2\Delta\omega^2\rangle_{\text{av } 5/2\leftrightarrow 7/2}=\frac{4[2I^2(I+1)^2-37I(I+1)+(1661/8)]}{2(2I+1)}\sum_j C_{jk}^2+\tfrac{1}{3}I(I+1)\sum_j D_{jk}^2-\frac{(2I-5)(2I+7)}{2(2I+1)}\times\sum_j C_{jk}D_{jk}, \quad (15c)$$

$$\langle\hbar^2\Delta\omega^2\rangle_{\text{av } 7/2\leftrightarrow 9/2}=\frac{4[2I^2(I+1)^2-65I(I+1)+(4741/8)]}{2(2I+1)}\sum_j C_{jk}^2+\tfrac{1}{3}I(I+1)\sum_j D_{jk}^2-\frac{(2I-7)(2I+9)}{2(2I+1)}\times\sum_j C_{jk}D_{jk}, \quad (15d)$$

and for NAR 2

$$\langle\hbar^2\Delta\omega^2\rangle_{\text{av } 3/2\leftrightarrow -1/2}=\frac{[2I^2(I+1)^2-9I(I+1)+(125/8)]}{2I+1}\times\sum_j C_{jk}^2+\frac{4I(I+1)}{3}\sum_j D_{jk}^2, \quad (16a)$$

$$\langle\hbar^2\Delta\omega^2\rangle_{\text{av } 5/2\leftrightarrow 1/2}=\frac{[2I^2(I+1)^2-17I(I+1)+(685/8)]}{2I+1}\times\sum_j C_{jk}^2+\frac{4I(I+1)}{3}\sum_j D_{jk}^2, \quad (16b)$$

$$\langle\hbar^2\Delta\omega^2\rangle_{\text{av } 7/2\leftrightarrow 3/2}=\frac{[2I^2(I+1)^2-33I(I+1)+(2189/8)]}{2I+1}\times\sum_j C_{jk}^2+\frac{4I(I+1)}{3}\sum_j D_{jk}^2, \quad (16c)$$

$$\langle\hbar^2\Delta\omega^2\rangle_{\text{av } 9/2\leftrightarrow 5/2}=\frac{[2I^2(I+1)^2-57I(I+1)+(5405/8)]}{2I+1}\times\sum_j C_{jk}^2+\frac{4I(I+1)}{3}\sum_j D_{jk}^2, \quad (16d)$$

where

$$C_{jk}=\tfrac{1}{2}(-B_{jk}+A_{jk}), \quad (17a)$$

$$D_{jk}=2B_{jk}+A_{jk}. \quad (17b)$$

From Eqs. (15) and (16) for the condition that $|A_{jk}|>|B_{jk}|$, we observe that the second moments for transitions between energy levels with the larger $|m|$ are *less* than the zero-field-gradient values. With knowledge of the shape of the transitions given by Eqs. (15) and (16) and the relative transition probabilities given in Tables I–IV, it is possible to construct the composite resonance line shape under the condition of a uniform field gradient.

III. EXPERIMENTAL CONDITIONS AND DATA

A. $A^{III}B^{V}$ Samples

Some important properties of the samples used in this investigation are shown in Table V. The suppliers of the crystals prepared InSb, InAs, GaSb, and AlSb by the Czochralski technique with growth along a [111] direction. The crystal of GaAs was prepared by the horizontal gradient-free method. Hall coefficient, resistivity, and etch pit measurements were made by the supplier on slices with (111) faces taken from the initial ingots. Emission spectra investigations for impurities were made by the supplier for crystals similar to those used in this experiment. These investigations indicate impurity content exclusive of dopants for all of the samples is at least a factor of 10 less than measured hole or electron concentrations of Table V, except for InSb. The impurity content for the InSb samples exclusive of dopants is less than one part in 10^7.

For the NAR investigations, crystals were prepared with a pair of (110) and (111) faces. The shape of the samples is an approximate cube with 1.7-cm side. Such preparation involved slow cutting of the crystals with a diamond slicing wheel and slow grinding of the crystal faces with 50- to 1-μ Al_2O_3 grit on cast iron and lead laps. Etch pit counts made after our preparation showed no change from the etch pit count made by the supplier. Since the original impurity concentration determinations, the samples have not been heated above 150°C. The sample faces were determined with x-ray diffractometer techniques to be within ± 10 min of arc of the desired crystal plane. The prepared faces are estimated to be within ± 20 min of arc of the desired crystal plane.

B. Experimental Method

Experimental line shapes were studied by NAR and NMR using the experimental technique and equipment previously described.[16] Each nuclear-spin system was studied using NAR 1, NAR 2, and NMR at a constant frequency between 8 and 10 MHz. The sample temperature for these measurements was 300°K. Acoustic waves were propagated along [110] and [111] directions, and the magnetic field was rotated in either a (001) or a ($\bar{1}$10) plane for NAR. For the NMR measurements, the rf magnetic-field component H_1 was along a [110] direction, and the plane of magnetic-field rotation was the (110). Saturation levels of NAR and NMR for a particular nuclear-spin system were determined, and the linewidth and line-shape measurements were made under conditions of less than 1% saturation. The magnetic-field modulation was 100 cps, and the amplitude of the field modulation was chosen to be no larger than one-eighth of the measured peak-to-peak resonance line-shape first derivative.

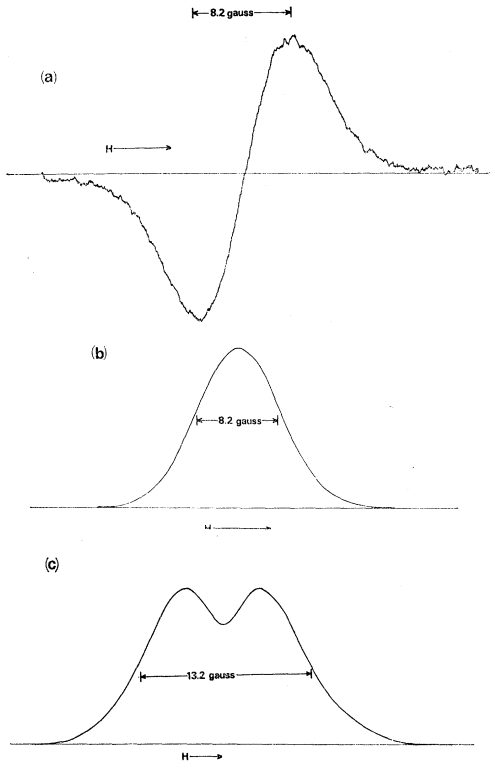

FIG. 1. $In^{115}As$ NAR 1 line shapes: (a) experimental first derivative for H along ⟨001⟩, (b) integrated experimental line shape for H along ⟨001⟩, (c) integrated experimental line shape for H along ⟨110⟩.

TABLE VI. Relevant nuclear properties.[a]

Nucleus	Natural abundance (%)	I	Magnetic moment (μ_N)	Electric quadrupole moment (10^{-24} cm^2)
Al^{27}	100.0	$\frac{5}{2}$	3.6385	0.149 ± 0.002[b]
Ga^{69}	60.2	$\frac{3}{2}$	2.0108	0.190 ± 0.001[c]
As^{75}	100.0	$\frac{3}{2}$	1.4349	$0.32\ \pm0.05$[d]
In^{113}	4.16	$\frac{9}{2}$	5.4960	0.820 ± 0.001[c]
In^{115}	95.84	$\frac{9}{2}$	5.5073	0.834 ± 0.001[c]
Sb^{121}	57.25	$\frac{5}{2}$	3.3417	$-0.53\ \pm0.08$[e]
Sb^{123}	42.75	$\frac{7}{2}$	2.5334	$-0.68\ \pm0.10$[e]

[a] F. Bovey and A. Tiers, *NMR Tables* (Wiley-Interscience, Inc., New York, 1967), 5th ed.
[b] H. Lew and G. Wessel, Phys. Rev. **90**, 1 (1953).
[c] G. F. Koster, Phys. Rev. **86**, 148 (1952).
[d] K. Murakawa, Phys. Rev. **110**, 393 (1958).
[e] K. Murakawa, Phys. Rev. **100**, 1369 (1955).

Relevant nuclear properties for the compounds investigated by NAR and NMR are given in Table VI. We did not observe that $Al^{27}Sb$ NAR, and the $Ga^{71}As$ and $Ga^{71}Sb$ NAR line shapes had too small signal-to-noise ratios to be useful. Because of small signal-to-noise ratios, we observed bulk crystal NMR only for $In^{113,115}As$, $In^{113,115}Sb$, $Ga^{69}As^{75}$, $Ga^{69}Sb^{121}$, and $Al^{27}Sb^{121}$.

C. Experimental Data

In the remainder of this paper, we refer to linewidths measured with the magnetic field along ⟨001⟩ directions

TABLE VII. Experimental linewidths and second moments for NAR 1, NMR, and NAR 2 when the external magnetic field is along ⟨001⟩ crystal directions.

Nucleus	NAR 1 δH_{pp} (G)	NAR 1 S_2 (G²)	NMR δH_{pp} (G)	NMR S_2 (G²)	NAR 2 δH_{pp} (G)	NAR 2 S_2 (G²)
$In^{113}As$	4.0 ±0.3	4.0 ±0.6	2.0 ±0.5	1.0 ±0.5	3.7 ±0.3	3.4 ±0.6
$In^{115}As$	8.2 ±0.2	17.2 ±0.4	1.9 ±0.1	2.8 ±0.2	4.85±0.10	5.86±0.10
$InAs^{75}$	8.0 ±0.2	16.0 ±0.4	8.4 ±0.3[a]	17.6 ±2[a]	8.0 ±0.2	16.0 ±0.8
$In^{113}Sb$(2)	11.9 ±1.0	33.5 ±6				
$In^{115}Sb$(2)	13.6 ±0.3	40.2 ±0.8	9.2 ±0.2	24 ±1	11.6 ±0.3	30.8 ±0.6
$InSb^{121}$(2)	17.5 ±0.3	74.9 ±2	17.5 ±1[b]	65 ±4[b]	17.0 ±0.4	72.5 ±2
$InSb^{123}$(2)					17.3 ±0.4	73.0 ±2
$Ga^{69}As$	1.73±0.06	0.75±0.02	1.64±0.05	0.56±0.02	1.53±0.04	0.59±0.02
$GaAs^{75}$	1.96±0.06	0.96±0.02	1.96±0.06	0.90±0.02	1.82±0.04	0.83±0.04
$Ga^{69}Sb$	4.6 ±0.2	5.3 ±0.3	4.9 ±0.2	6.0 ±0.4	4.1 ±0.1	4.2 ±0.2
$GaSb^{121}$	5.3 ±0.1	5.6 ±0.1	4.1 ±0.1	3.9 ±0.1	4.2 ±0.1	3.9 ±0.2
$GaSb^{123}$					4.2 ±0.1	4.4 ±0.1
$Al^{27}Sb$			2.21±0.05	0.73±0.02		
$AlSb^{121}$	2.09±0.05	1.21±0.1	1.29±0.03	0.42±0.03	1.26±0.03	0.46±0.01
$AlSb^{123}$					1.32±0.03	0.54±0.06

[a] Reference 2.
[b] Reference 1.

as ⟨001⟩ linewidths. A similar meaning is given to the phrase ⟨110⟩ linewidths.

The experimental NAR and NMR linewidths and generally the line shapes exhibit large anisotropic behavior as the direction of the external magnetic field is varied with respect to the crystalline axes. All ⟨001⟩ linewidths for a given nuclear-spin system observed by a particular resonance transition have the same minimum magnitudes, and the line shapes are close to Gaussian functions. Away from the resonance center, the experimental line shapes may have slightly smaller amplitudes than a Gaussian function. Such linewidths are in all cases larger than calculated dipole-dipole widths. The NAR 1 linewidths are greater or equal to the NAR 2 linewidths, which are greater or equal to the NMR linewidths.

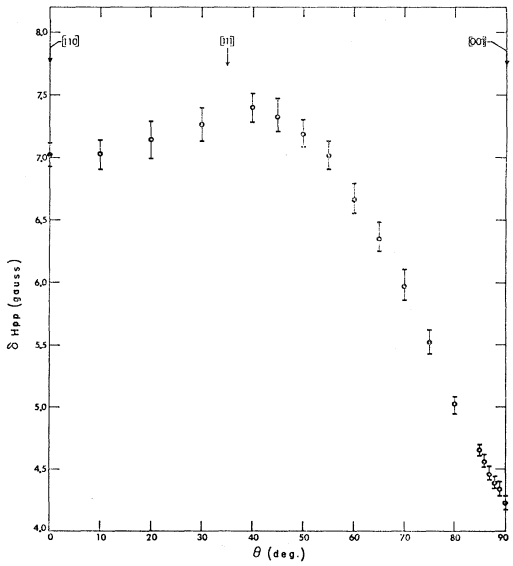

FIG. 2. $GaSb^{123}$ NAR 2 experimental peak-to-peak linewidths, δH_{pp}, as a function of Θ, the angle measured in the $(1\bar{1}0)$ plane from the [110] crystal direction to the direction of H.

When the magnetic field is rotated from ⟨001⟩ directions, the linewidths broaden and the line shapes generally depart from Gaussian functions. In particular, all ⟨110⟩ linewidths for a given nuclear-spin system observed by a particular resonance transition have the same magnitudes, and the line shapes are identical and depart from Gaussian functions. Away from the resonance center the experimental linewidths decrease in amplitude more slowly than a Gaussian function. Also, for the NAR 1 of $In^{115}As$, $GaSb^{121}$, and $AlSb^{121}$, a symmetric splitting of the resonance line shape occurs. The magnitudes of the NAR 1 linewidths are larger than the NAR 2 linewidths, which are generally larger than the NMR linewidths.

To illustrate typical measured linewidths and line shapes, the $In^{115}As$ NAR 1 is shown in Fig. 1. The experimental first derivative of the ⟨001⟩ resonance line shape is shown in Fig. 1(a). Figures 1(b) and 1(c) show the integrated experimental first derivative ⟨001⟩ and ⟨110⟩ line shapes, respectively. The line shape of Fig. 1(c) is the most striking example of an anisotropy that is a common property of each of the nuclear-spin systems. In Fig. 2, the peak-to-peak linewidth of $GaSb^{123}$ NAR 2 is plotted as a function of the angle Θ in the $(1\bar{1}0)$ plane between the direction of the external magnetic field and the [110] crystal direction. In Fig. 3, the peak-to-peak linewidth of $AlSb^{123}$ NAR 2 is plotted as a function of the angle Φ in the (001) plane between the direction of the magnetic field and the [110] axis. We notice in both Figs. (2) and (3) the very sharp minimum in the ⟨001⟩ linewidths.

In Table VII, we list the measured ⟨001⟩ peak-to-peak

TABLE VIII. Experimental NAR 1 and NAR 2 linewidths and second moments and NMR linewidths when the external magnetic field is along ⟨110⟩ crystal directions.

Nucleus	NAR 1 δH_{pp} (G)	S_2 (G²)	NMR δH_{pp} (G)	NAR 2 δH_{pp} (G)	S_2 (G²)
$In^{115}As$	13.4 ±0.3		2.5 ±0.2	5.80±0.1	8.40±0.3
$InAs^{75}$	12.2 ±0.3	37.2 ±0.8		10.1 ±0.3	25.2 ±0.5
$In^{115}Sb$(2)	16.0 ±0.4	56.0 ±1.0	9.8 ±0.2	12.2 ±0.3	33.9 ±0.8
$InSb^{121}$(2)	19.4 ±0.4	94.2 ±0.9		18.4 ±0.4	84.7 ±2.0
$Ga^{69}As$	3.34±0.08	2.79±0.10	2.18±0.06		
$GaAs^{75}$	6.60±0.10	13.6 ±0.4	2.41±0.04	3.90±0.09	4.73±0.10
$Ga^{69}Sb$	5.7 ±0.1	8.1 ±0.4	5.6 ±0.2		
$GaSb^{121}$	10.0 ±0.3	61.5 ±1.0	4.2 ±0.2	5.75±0.20	22.4 ±0.6
$Al^{27}Sb$			3.23±0.08		
$AlSb^{121}$	4.95±0.10	15.4 ±0.4	2.40±0.06	3.01±0.08	5.9 ±0.2

linewidths, δh_{pp}, and second moments, S_2, determined from the experimental line shapes. The second moments are computed using the formula[21]

$$S_2=\langle\Delta H^2\rangle_{av}=\frac{1}{3}\int_{-\infty}^{\infty}(H-H_0)^3\frac{dI}{dH}dH\Big/\int_{-\infty}^{\infty}(H-H_0)\frac{dI}{dH}dH, \quad (18)$$

where dI/dH is the experimental amplitude for the resonance line-shape first derivative, and H_0 is the magnetic field at the resonance line center. The NMR line shapes that we measure have an asymmetry characteristic of a mixture of the real and imaginary parts of the nuclear-spin susceptibility.[22] The amount of asymmetry, however, is small because of skin depths for 10-MHz rf fields of approximately 0.2–2.0 cm for our samples. The NMR linewidths that we report are the peak-to-peak separation of such asymmetric line shapes.

In Table VIII, we list the peak-to-peak ⟨110⟩ experimental NAR and NMR linewidths δH_{pp}, and the ⟨110⟩ NAR second moments, S_2. By integrating the ⟨110⟩ and ⟨001⟩ line shapes for each nuclear-spin system, we find that within an experimental error of ±3% the same number of nuclear spins contributes to both line shapes, except for $In^{115}As$. The $In^{115}As$, ⟨110⟩ line shape contains contributions from only 85% of the nuclear spins contributing to the ⟨001⟩ line shape.

In Table IX, we list a comparison of the $InSb^{121}$ NAR 1 ⟨001⟩ and ⟨110⟩ linewidths and second moments for three samples having carrier concentrations over a range of 10^{14} to 10^{17} carriers cm^{-3}. We notice that the ⟨001⟩ second moments are identical and the ⟨110⟩ second moments increase with increasing carrier concentrations.

In Table X, we list the computed ⟨001⟩ and ⟨110⟩ dipole-dipole NAR 1 and NAR 2 second moments. These values were determined using the B_{jk}^2 and $\tilde{B}_{jk}^2$ terms in Eqs. (7) and (8) and the values of the zinc-blende lattice sums given in Sec. II. The NAR 1 dipole-dipole second moments are also equal to the NMR dipole-dipole second moments, as we have noted in Sec. II.

TABLE IX. Experimental NAR 1 linewidths and second moments of $InSb^{121}$ in InSb crystals with different charge carrier concentrations.

Sample	H along ⟨001⟩ δH_{pp} (G)	S_2 (G²)	H along ⟨110⟩ δH_{pp} (G)	S_2 (G²)
InSb(1)	17.5±0.4	75±2	18.6±0.4	83±2
InSb(2)	17.5±0.4	75±2	19.4±0.4	94±2
InSb(3)	17.5±0.4	77±2	26.6±0.6	198±4

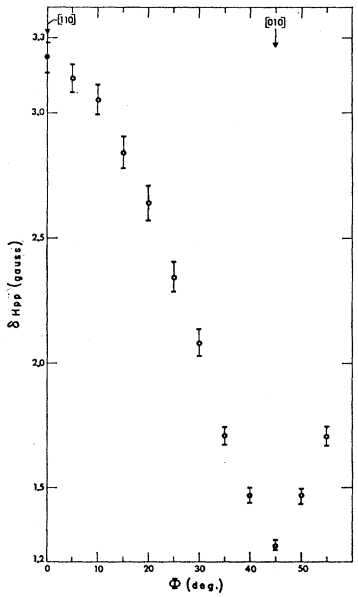

FIG. 3. $AlSb^{123}$ NAR 2 experimental peak-to-peak linewidths, δH_{pp}, as a function of Φ, the angle measured in the (001) plane from the [110] crystal direction to the direction of H.

[21] G. E. Pake and E. M. Purcell, Phys. Rev. 74, 1184 (1948).
[22] A. C. Chapman, P. Rhodes, and E. F. Seymour, Proc. Phys. Soc. (London) 370, 345 (1957).

TABLE X. Calculated relevant dipole-dipole NAR 1 and NAR 2 second moments for H along ⟨001⟩ and along ⟨110⟩.

Nucleus	NAR 1 S_2 (G²) ⟨001⟩	S_2 (G²) ⟨110⟩	NAR 2 S_2 (G²) ⟨001⟩	S_2 (G²) ⟨110⟩
$In^{113}As$	0.491	1.042	0.471	
$In^{115}As$	0.994	1.761	0.521	1.085
$InAs^{75}$	0.412	4.259	0.366	4.193
$In^{113}Sb$	0.381			
$In^{115}Sb$	0.717	1.851	0.401	1.401
$InSb^{121}$	0.402	3.028	0.322	2.915
$InSb^{123}$			0.317	2.907
$Ga^{69}As$	0.286	0.924	0.204	0.807
$GaAs^{75}$	0.248	1.613	0.179	1.514
$Ga^{69}Sb$	0.258	1.560	0.206	1.485
$GaSb^{121}$	0.340	1.287	0.225	1.123
$GaSb^{123}$			0.217	1.111
$Al^{27}Sb$	0.558	1.943		
$AlSb^{121}$	0.408	2.285	0.298	2.127
$AlSb^{123}$			0.290	2.116

The NAR linewidths and line shapes that we list in Tables VII–IX are independent of the acoustic wave propagation and the polarization directions that we have used. Therefore, the only effect of the nonsaturating acoustic wave is to allow observation of the resonant spin-phonon interaction, and the line broadening is determined by the nuclear environment. We also have found that the NAR linewidth and line shapes are independent of resonance frequency between 8.2 and 10.7 MHz. Therefore, the linewidth broadening mechanisms are magnetic-field-independent.

IV. ANALYSIS OF RESONANCE LINE SHAPES AND LINEWIDTHS

A. Determination of Dominant Broadening Mechanisms

The five $A^{III}B^{V}$ compounds that we have investigated have similar lattice constants and similar chemical bonding.[23] For the five samples of Tables VII and VIII, the charge carrier concentrations listed in Table V are all within an order of magnitude of each other. Therefore, the impurity concentrations are very small and approximately equal in the five compounds. It is reasonable to expect that the nuclear environments will be similar at B nuclear positions and at A nuclear positions in the five compounds. Tables VII, VIII, and X show that the differences between either the ⟨001⟩ or ⟨110⟩ experimental second moments and the computed dipole-dipole second moments are largest for those nuclear-spin systems with largest atomic numbers and largest quadrupole moments. We make use of these large atomic numbers, large quadrupole moment nuclear-spin systems in the following analysis of the line broadening. We then generalize these results for the smaller atomic number, smaller quadrupole moment nuclear-spin systems. First, we consider the ⟨001⟩ line broadening mechanisms and then the source of the anisotropic broadening.

By studying the NAR 1, NAR 2, and NMR ⟨001⟩ second moments of $In^{113,115}As$ and $In^{113,115}Sb$, it is possible to make use of the second-moment analysis of Sec. II to determine which broadening mechanisms are dominant. Broadening of the ⟨001⟩ second moments beyond the dipole-dipole second moments must be due to interactions independent of the magnetic-field magnitude. Likely possibilities in such large atomic-number atom solids are the quadrupole,[18] pseudodipolar,[4] and nuclear exchange[1,3,5] interactions. Expressions for the quadrupole and exchange second moments have already been given in Eqs. (7), (8), and (10). The Hamiltonian for the pseudodipolar interaction can be written[4]

$$\mathcal{H}_{Pd}=\sum_{j<k} D_{jk}[\mathbf{I}_j\cdot\mathbf{I}_k-3r_{jk}^{-2}(\mathbf{I}_j\cdot\mathbf{r}_{jk})(\mathbf{I}_k\cdot\mathbf{r}_{jk})], \quad (19)$$

where D_{jk} is the interaction constant. The pseudodipolar interaction has the same nuclear-spin operator dependence as the ordinary dipole-dipole interaction and should produce the same second-moment dependence on the angle between the external magnetic field and the crystal axes. Therefore, the comparisons of Sec. II for the dipole-dipole second moments can be used for expected pseudodipolar second moments.

From Table VII, the ratio of NAR 1 to NMR In^{115} ⟨001⟩ second moments for InAs is 17.2/2.8=6.2, and for InSb is 40.2/24.0=1.8. These ratios are in disagreement with the ratio of 1.00 predicted by the comparisons of Sec. II for dipole-dipole and, therefore, pseudodipolar second moments. The ratio of In^{115} to In^{113} NAR 1 second moments for InAs is 17.2/4.0=4.3 and for InSb 40.2/33.5=1.2. Because In^{113} and In^{115} have the same spin and very similar nuclear properties, the predicted quadrupole second-moment ratio is 1.0. We conclude that the quadrupole or the pseudodipolar interactions cannot alone explain the $In^{113,115}$ resonance second moments.

Nuclear exchange can explain the $In^{113,115}$ second moments. The larger NAR 1 than NMR In^{115} second moment can be understood as due to contributions from both like-spin and unlike-spin exchange interactions for NAR 1, and due to a contribution from only unlike-spin exchange interactions for NMR. The larger In^{115} than In^{113} second moment can be understood as due to a larger like-spin than unlike-spin exchange for the In nucleus, and by more neighboring like spins for In^{115} than for In^{113}. Because of the greatly different $In^{115,113}$ natural abundances, each $In^{115}As$ nucleus has four unlike As nuclei as nearest neighbors and approximately 12 *like* In^{115} nuclei as next nearest neighbors. Each $In^{113}As$ nucleus has four unlike As nuclei as nearest neighbors and approximately 12 *unlike* In^{115} nuclei as next nearest neighbors.

Similar comparisons can also be made for the other

[23] O. Madelung, *Physics of III-V Compounds* (John Wiley & Son, Inc., New York, 1964).

nuclear-spin systems in Table VII. The conclusion is that exchange interactions are dominant over quadrupole and pseudodipolar interactions in the broadening of ⟨001⟩ second moments. We show below that exchange and dipole-dipole interactions alone quantitatively explain ⟨001⟩ second moments.

Next we consider the source of the additional broadening which results for each of the nuclear-spin systems when the magnetic field is rotated from ⟨001⟩ directions. As noted in Sec. III, $In^{115}As$, $GaSb^{121}$, and $AlSb^{121}$ all show a symmetric ⟨110⟩ line-shape splitting. The In^{115} As NAR 1 line shape begins to split at angles as small as 5° between the direction of the magnetic field and ⟨001⟩ directions. Furthermore, the $In^{115}As$ line-shape splitting agrees qualitatively with the peak-to-peak linewidths plotted in Figs. 2 and 3 for different nuclear-spin systems. The $In^{115}As$ NAR 2 and NMR ⟨110⟩ line shapes are broadened over the ⟨001⟩ line shapes, but they show no signs of splitting. Such a splitting of the NAR 1 but not of the NAR 2 and NMR line shapes is understood from the discussion in Sec. II relating to the quadrupole interaction. We conclude that the broadening of the NAR and NMR linewidths in directions for the magnetic field other than the ⟨001⟩ directions is due to an anisotropic quadrupole interaction and a generally smaller anisotropic dipole-dipole interaction. Such identification of the anisotropic broadening allows us to say that the dominant exchange broadening for ⟨001⟩ second moments is isotropic. We show below that isotropic exchange, anisotropic dipole-dipole, and anisotropic quadrupole interactions quantitatively explain the ⟨110⟩ second moments.

B. Nuclear Exchange

In Sec. IV A, nuclear isotropic exchange between like and unlike spins has been shown to qualitatively explain the $In^{113,115}$ NAR and NMR ⟨001⟩ second moments. The fact that both like and unlike exchange interactions are present indicates that the exchange interaction is large enough to cause linewidth changes from as far as the second shell of nearest neighbors from the resonant nuclear spin. Such an observation means that we can investigate the dependence of the exchange constant on distance from the resonant nuclear spin. Let us assume that an exchange constant is as given in Eq. (13), except that the dependence on r_{jk} is r_{jk}^{-n} rather than r_{jk}^{-4}. Then, the ratio of like to unlike exchange constants for $In^{115}Sb$ can be written

$$\frac{A_{\mathrm{InIn}}}{A_{\mathrm{InSb}}}=(\gamma_{\mathrm{In}}/\gamma_{\mathrm{Sb}})\left(\frac{\zeta_{\mathrm{In}}\Psi_{\mathrm{In}}^{2}(0)}{\zeta_{\mathrm{Sb}}\Psi_{\mathrm{Sb}}^{2}(0)}\right)(a/a')^{n}, \qquad (20)$$

where a is the distance to the first shell of neighbors, and a' is the distance to the second shell of neighbors. By subtracting the computed dipole-dipole second moments from the experimental $In^{115}Sb$ NAR 1 and NAR 2 ⟨001⟩ second moments, we obtain exchange second moments. These values are set equal to the exchange contributions in Eqs. (7) and (8). The sum for like neighbors in these equations is computed for the 12 second neighbors at a distance $a'=(\frac{1}{4}\sqrt{8})\ a_0$, and the sum for unlike neighbors is computed over the Sb^{121} and Sb^{123} nuclei that are first neighbors at a distance $a=\frac{1}{4}\sqrt{3}\ a_0$. The exchange constants A_{InIn} and A_{InSb} can then be determined. Gueron[24] has measured the wave-function density ratio for electrons at the bottom of the conduction band in InSb as $\Psi_{\mathrm{Sb}}^{2}/\Psi_{\mathrm{In}}^{2}=1.70$. With this wave-function density ratio and the exchange constants, Eq. (20) is solved for the value of $n=4.4\pm0.5$.

We can follow a similar procedure to calculate $A_{\mathrm{InIn}}/A_{\mathrm{InAs}}$. In this case, no measured values of the s-character electronic wave-function densities are known for the In and As nuclear positions. To estimate the ratio of wave-function densities at the nuclear positions of In and As, we choose the ratio of atomic numbers. Such a choice is not unreasonable on the basis of the Fermi-Segré[25] formula for wave-function densities. The value of $n=4$ is found from an equation for $In^{115}As$ similar to Eq. (20). We conclude that the dependence of the experimentally derived exchange constants on internuclear distance agrees with that of Anderson's exchange constant, Eq. (13), and therefore supports his theory[1,5] for indirect nuclear exchange in semiconductors.

Additional support for the Anderson theory is seen in the identical NAR 1 ⟨001⟩ $InSb^{121}$ second moments shown in Table IX. The three InSb samples have hole and electron carrier concentrations that vary from 10^{14} to 10^{17} cm^{-3}. There is no dependence of the measured second moment on hole or electron carrier concentration. This observation is in agreement with the theory of Anderson,[1] which states that the excited states of *binding electrons* in semiconductors interact with the nuclear spins via the hyperfine interaction.

The exchange constant of Anderson is now used to analyze the ⟨001⟩ second moments. The second-moment expressions in Eqs. (7), (8), and (10) involve sums of the square of the exchange constants over the nuclear positions around the resonant nuclear spin. It is easy to show for such a compound as InAs that 98% of the sum for the unlike-spin exchange constant comes from the shell of first neighbors, and 96% of the sum for the like-spin exchange constant comes from the shell of second neighbors. Therefore, in the analysis described below, we consider only sums over first and second nearest neighbors.

We now consider the cross term sums involving $A_{jk}B_{jk}$ and $\tilde{A}_{jk}\tilde{B}_{jk}$ in Eqs. (7) and (8). Because of the r_{jk}^{-7} dependence of the cross products, the major contribution to the sum involving $\tilde{A}_{jk}\tilde{B}_{jk}$ comes from the first shell of neighbors, and to the sum over $A_{jk}B_{jk}$ from the second shell of neighbors. If the nuclear spins

[24] M. Gueron, Phys. Rev. **135**, A200 (1964).
[25] E. Femi and E. Segré, Z. Physik **82**, 729 (1933).

TABLE XI. Values of the exchange term a_{jk}^2 computed from the experimental ⟨001⟩ second moments.

Compound	$a_{jk}^2(10^{-14}$ cm$^2)$
InAs	$a^2_{\mathrm{InIn}}=0.76\pm0.08$
	$a^2_{\mathrm{InAs}}=0.29\pm0.03$
InSb	$a^2_{\mathrm{InIn}}=1.3\pm0.1$
	$a^2_{\mathrm{InSb}}=2.2\pm0.2$
GaAs	$a^2_{\mathrm{GaGa}}=0.026\pm0.003$
	$a^2_{\mathrm{GaAs}}=0.026\pm0.003$
	$a^2_{\mathrm{AsAs}}=0.026\pm0.003$
GaSb	$a^2_{\mathrm{GaSb}}=0.25\pm0.04$
	$a^2_{\mathrm{SbSb}}=0.48\pm0.08$
AlSb	$a^2_{\mathrm{AlSb}}\simeq0$
	$a^2_{\mathrm{SbSb}}=0.20\pm0.05$

of either shell are identical, then the sum of the cross terms over that shell is zero. If two nuclear isotopes are present in the first or second shell of neighbors, the sums of the cross terms may not be zero for a particular resonant nuclear position. Because of the $\frac{3}{2}\cos^2\theta_{jk}-\frac{1}{2}$ terms in B_{jk} and $\tilde{B}_{jk}$, the measured average second-moment contribution from all of the resonant nuclear spins will involve an average zero contribution from the cross terms.

Previous determinations of the exchange constant for NMR exchange broadened line shapes[1,2] have been carried out by constructing theoretical line shapes from numerically determined exchange interactions to nearest unlike neighbors. Because we consider not only exchange interactions between first but also second neighbors, we use a direct comparison between the experimentally determined ⟨001⟩ second moments and the theoretical expressions given by Eqs. (7) and (8).

For convenience in analyzing the exchange contributions to the ⟨001⟩ second moments, we write Anderson's exchange constant, Eq. (13), as

$$A_{jk}=a_{jk}\gamma_j\gamma_k\hbar^2r_{jk}^{-4}, \tag{21}$$

where

$$a_{jk}=(8/9\pi)\gamma_e^2\Omega^2\zeta_j\Psi_j^2(0)\zeta_k\Psi_k^2(0)m^*. \tag{22}$$

The ⟨001⟩ second moments due to exchange can be written explicitly from Eqs. (7) and (8) as

$$S_{2\,\mathrm{NAR}\,1}=\tfrac{1}{3}S(S+1)\sum_j\tilde{a}_{jk}^2\gamma_S^2\hbar^2r_{jk}^{-8}+2I(I+1)\sum_j a_{jk}^2\gamma_I^2\hbar^2r_{jk}^{-8}, \tag{23}$$

$$S_{2\,\mathrm{NAR}\,2}=\tfrac{1}{3}S(S+1)\sum_j\tilde{a}_{jk}^2\gamma_S^2\hbar^2r_{jk}^{-8}+\tfrac{1}{2}I(I+1)\sum_j a_{jk}^2\gamma_I^2\hbar^2r_{jk}^{-8}, \tag{24}$$

where the sum which includes $\tilde{a}_{jk}^2$ is for the four first neighbors, and the sum which includes a_{jk}^2 is for the 12 second neighbors. By subtracting the computed dipole-dipole second moments from the experimentally determined ⟨001⟩ second moments, we can use these exchange second moments with Eqs. (23) and (24) to determine a_{jk}^2 and $\tilde{a}_{jk}^2$. In such computations for the five compounds of Table VII, there is good agreement for $\tilde{a}_{jk}^2$ determined for a given compound at A and B nuclear positions. The computed values of a_{jk}^2 and $\tilde{a}_{jk}^2$ are given in Table XI. In this Table, some like-spin values of a_{jk}^2 are missing because of the inability to determine them accurately from the ⟨001⟩ second moments.

The exchange constants which are computed from the NAR second moments and shown in Table XI also predict the measured NMR ⟨001⟩ exchange second moments within experimental error. However, for several nuclear-spin systems, the NMR peak-to-peak linewidth is *narrower* than that computed from the measured second moment assuming a Gaussian function for the line shape. This effect is most evident for the $In^{115}As$ ⟨001⟩ NMR where the peak-to-peak width is 1.90 G, and the second moment is 2.80 G^2. An explanation of this small peak-to-peak width is that like-spin exchange, while not affecting the second moment, does increase the fourth moment of the line shape. Van Vleck[14] predicts such an "exchange narrowing" due to terms of the form $A_{jk}^2B_{jk}^2$ in the NMR fourth moment.

The s-character electronic wave-function density in the solid $\zeta_j\Psi_j^2(0)$ at both A and B nuclear positions of a given compound can be determined if an assumption about the effective mass is made. We assume that the effective mass for these large momentum electrons is the free-electron mass. The wave-function densities are easily computed from Eq. (22) and the values of Table XI. Such computed wave-function densities are listed in Table XII. The magnitudes of the wave-function densities for InSb from Table XII can be compared with the magnitudes measured by Gueron[24] for conduction electrons. Gueron finds values of $\Psi_{\mathrm{Sb}}^2=15.9\times10^{25}$ cm^{-3} and $\Psi_{\mathrm{In}}^2=9.3\times10^{25}$ cm^{-3}, which are between three and four times larger than the computed larger momentum electron values of Table XII. Also in Table XII, we notice that the ratio between the wave-function density at A and B nuclear positions in the same compound is quite close the ratio of atomic numbers, except of InSb. Such a proportionality is again expected on the basis of the Fermi-Segrè[25] formula for wave-function densities.

TABLE XII. Values of the electronic wave-function density in the solid, $\zeta_j\Psi_j^2(0)$, computed from the exchange constants.

Compound	Nucleus	$\zeta_j\Psi_j^2(0)$ $(10^{25}$ cm$^{-3})$
InAs	In	3.7 ± 0.2
	As	2.3 ± 0.2
InSb	In	3.5 ± 0.2
	Sb	4.5 ± 0.4
GaAs	Ga	2.0 ± 0.2
	As	2.0 ± 0.2
GaSb	Ga	2.3 ± 0.3
	Sb	3.5 ± 0.6
AlSb	Al	≈0
	Sb	2.6 ± 0.8

C. Quadrupole Broadening

In this section, we first show that the quadrupole broadening is due to a distribution of field gradients. We then characterize the broadening in terms of a root-mean-square field gradient for each of the nuclear-spin systems except $Al^{27}Sb$. Finally, we determine the probable source of the field gradients and estimate the ratios of antishielding constants between In, As, Ga, and Sb.

It is possible to construct a quadrupole broadened resonance line shape for a given nuclear-spin system by using the quadrupole splittings and transition probabilities of Tables I–IV and the second moments for these transitions determined from Eqs. (15) and (16). Such a computed resonance line shape is for a particular resonant spin or for a sample of resonant spins under a uniform field gradient. An assumption must also be made about the shape of the resonance line shape of a particular transition.

We have programmed an IBM 7072 computer to determine the NAR ⟨110⟩ line shapes as a function of the field gradient producing quadrupole splittings. In such a program, we have assumed that the NAR transitions are Gaussian functions and have used computed values of ⟨110⟩ dipole-dipole second moments and isotropic exchange second moments. We compare the experimental line shape with the particular computed first derivative of the quadrupole broadened line shape which agrees with the experimental peak-to-peak width. Such comparisons are made in Figs. 4(a) and 4(b). We notice in Fig. 4(a) that the $GaAs^{75}$ NAR 1 ⟨110⟩ experimental line shape has a different shape and is much broader than the predicted theoretical line shape for a uniform field gradient. We conclude that a distribution of field gradients must be present. In Fig. 4(b), the $In^{115}As$ NAR 1 ⟨110⟩ experimental line shape is qualitatively explained by the theoretical shape for a uniform field gradient, except that the experimental shape is broader, indicating some distribution of field gradients. It is interesting to note that the splitting of the $In^{115}As$ NAR 1 ⟨110⟩ line shape occurs at a ratio of the ⟨110⟩ to ⟨001⟩ peak-to-peak linewidths of only 1.6. It is not possible to produce a theoretical quadrupole splitting of the over-all ⟨110⟩ line shape for such a ratio of split-to-unsplit linewidths except if the $\frac{5}{2}$–$\frac{7}{2}$ and $\frac{7}{2}$–$\frac{9}{2}$ transitions have line shapes with second moments appreciably narrower than the ⟨001⟩ second moment. Such a narrowing is predicted by the second moments for these transitions that we compute in Eqs. (15).

In order to characterize the distribution of field gradients at the nuclear positions, we choose to use the mean-square field gradient,

$$N^{-1}\sum_j V_{zzj}^2.$$

This field-gradient expression is computed from the

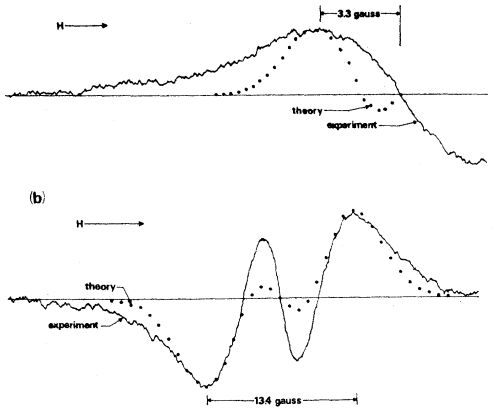

FIG. 4. Comparison of experimental and theoretical quadrupole broadened line shapes: (a) $GaAs^{75}$ NAR 1 ⟨110⟩ line shapes, (b) $In^{115}As$ NAR 1 ⟨110⟩ line shapes.

⟨110⟩ NAR second moments of Table VIII by subtracting the ⟨110⟩ dipole-dipole and exchange second moments from the experimental second moments. Consistent with this analysis, we find that NAR 1 and NAR 2 second moments for the same nuclear-spin system give the same mean-square field gradient. In Table XIII, we list the root-mean-square field gradients determined for the five samples of Table VIII and the two additional InSb samples of Table IX. We notice that the magnitudes of the root-mean-square field gradients are approximately equal for the five samples of Table VIII with approximately equal carrier concentrations. We notice too that the field gradients increase with increasing carrier concentration for the three InSb samples.

The electric field gradients that produce quadrupole broadening in the $A^{III}B^{V}$ compounds are characterized by magnitudes of the order of 10^{11} esu cm^{-3} for carrier concentrations of 10^{16} cm^{-3}. Another feature of the field gradients is the strongly anisotropic quadrupole broadening that they produce, as shown in Figs. 2 and 3. Simple considerations for the field gradients that

TABLE XIII. Root-mean-square field gradients at A and B nuclear positions computed from ⟨110⟩ quadrupole second moments.

Nucleus	$(N^{-1}\sum_j V_{zzj}^2)^{1/2}$ (10^{11} esu/cm^3)
$In^{115}As$	2.9±0.1
$InAs^{75}$	1.3±0.1
$InSb^{121}(1)$	2.2±0.1
$In^{115}Sb(2)$	4.4±0.2
$InSb^{121}(2)$	4.8±0.3
$InSb^{121}(3)$	11.0±0.5
$Ga^{69}As$	1.8±0.2
$GaAs^{75}$	2.2±0.1
$Ga^{69}Sb$	2.6±0.1
$GaSb^{121}$	7.3±0.2
$AlSb^{123}$	3.4±0.2

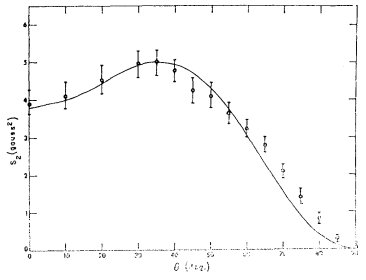

FIG. 5. Comparison with theory of the $In^{115}As$ NAR 2 quadrupole second moment as the magnetic field is rotated in the $(\bar{1}10)$ plane.

produce such anisotropic broadening indicate that the field gradients could be explained by strains along ⟨111⟩ directions. The root-mean-square field gradient ratio from Table XIII at the A and B nuclear positions in the same compound can be compared with the ratio of S-tensor components[16] at the same A and B nuclear positions. These S-tensor components characterize the field gradient produced by strain. The appropriate S tensor component[16] to associate with a strain in the ⟨111⟩ direction is S_{44}. We compare the ratio of the experimentally determined S_{44} components with the ratio of the root-mean-square field gradient at the same A and B nuclear positions. Unequal ratios for InAs, InSb, and GaAs and approximately equal ratios for GaSb are found. Our conclusion is that the common source of field gradients for all four of these compounds is not strain.

It is difficult to understand the anisotropy of the quadrupole broadening from any model which reduces the lattice to a continuum. Cohen and Reif[18] consider the electric field gradients produced by ions at large distances from the ion by replacing the actual lattice with a continuum approximation. Even to produce the magnitude of the measured field gradients of Table XIII on the basis of the continuum model would require ion concentrations two to three orders of magnitude larger than our measured carrier concentrations in the samples.

An explanation that agrees with the experimental data is that the electric field gradients are due to the electric fields of the ionized substitutional impurities. The strong anisotropy of the quadrupole broadening relative to the crystal axes can be explained by a general tensor relationship between electric field gradient components V_{ij} and the electric field components[26,27] E_k

$$V_{ij}=R_{ijk}E_k, \tag{25}$$

where R_{ijk} is a third-order tensor whose nonzero components are determined by the symmetry of the zinc-blende structure. It can be shown[27] that R_{ijk} has three identical nonzero components which we call R_{14}.

From known transformation properties of third-order tensors, we write Eq. (25) in the experimental reference frame, where x' is along $[110]$, y' is along $[\bar{1}10]$, and z' is along $[001]$. We then compute the field gradient component V_{zz} for magnetic-field rotation in the $(\bar{1}10)$ plane and the (001) plane, which are given in Eqs. (26) and (27), respectively. The angles Θ and Φ have the meanings given in Sec. III:

$$V_{zz}=R_{14}(E_z\cos^2\Theta+E_x\sin 2\Theta), \tag{26}$$

$$V_{zz}=R_{14}E_z\cos 2\Phi. \tag{27}$$

We notice in Eqs. (26) and (27) that the field gradients are zero for the magnetic field along ⟨001⟩ directions, in agreement with no experimental quadrupole broadening in such directions.

Equations (26) and (27) can be used to develop field-gradient expressions to compare with the measured quadrupole broadening anisotropy. In the second moment expressions of Eqs. (7) and (8) the field gradient enters as the sum of the squares of the field gradient component V_{zz} at each resonant nuclear spin. We assume that each resonant nucleus is affected by the electric field of no more than one ionic charge. The values of the square of the field gradient expressions in Eqs. (26) and (27) are computed for all nuclear spins in a spherical shell a distance r from a point charge e. We assume here that the appropriate electric field in a III-V semiconductor for electronic[28] polarization is e/r^2. Such a calculation gives the average square field-gradient dependence on angles Θ or Φ for all nuclear spins in the field of the point charge. Equation (28) gives the average square field-gradient expression for rotation in a $(\bar{1}10)$ plane and Eq. (29) for rotation in a (001) plane:

$$V_{zz\,\mathrm{av}}{}^2=\tfrac{1}{3}R_{14}{}^2e^2r^{-4}(\cos^4\Theta+\sin^2 2\Theta), \tag{28}$$

$$V_{zz\,\mathrm{av}}{}^2=\tfrac{1}{3}R_{14}{}^2e^2r^{-4}\cos^2 2\Phi. \tag{29}$$

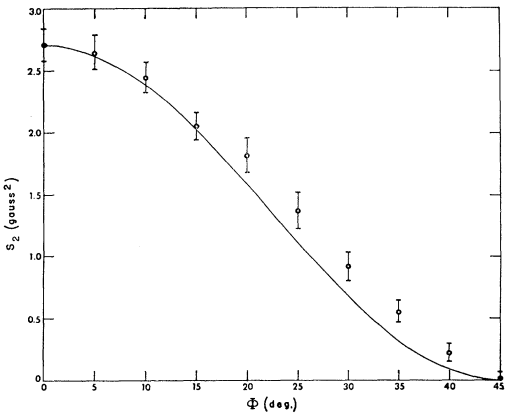

FIG. 6. Comparison with theory of the $GaAs^{75}$ NAR 2 quadrupole second moment as the magnetic field is rotated in the (001) plane.

[26] D. Gill and N. Bloembergen, Phys. Rev. **129**, 2398 (1963).
[27] E. Brun, R. J. Mahler, H. Mahon, and W. L. Pierce, Phys. Rev. **129**, 1965 (1963).
[28] H. D. Brodsky and E. Burnstein, Bull. Am. Phys. Soc. **7**, 214 (1962).

In Fig. 5, we plot the experimentally determined $In^{115}As$ NAR 2 quadrupole second moments and the angular dependence of Eq. (28) matched with the experimental value at $\Theta=35°$. In Fig. 6, we plot the $GaAs^{75}$ NAR 2 quadrupole second moments and the angular dependence of Eq. (29) matched to the experimental value at $\Phi=0°$. Considering the assumptions made to compute Eqs. (28) and (29), we conclude that the tensor relationship between electric field gradients and electric fields is in good agreement with the anisotropy of the experimental data.

The component R_{14} has been determined experimentally for GaAs by two different methods.[26,27] The static values[26] of R_{14} are 1.05×10^{10} cm^{-1} at the Ga^{69} nuclear position and 1.55×10^{10} cm^{-1} at the As^{75} nuclear position. We compare these values of R_{14} with those estimated using the computed mean-square field gradients, the carrier concentration, and the following model. We assume that the charge carrier concentration is the ionized impurity concentration and that these ions are uniformally distributed, each with charge e. The inter-ion separation is taken to be $2r_0$. We also assume that the root-mean-square field gradients that we compute in Table XIII characterize the field gradients at the nuclei in a shell at a radius r_0 from an ion. Most of the nuclear spins are in such shells around each ion. With the assumptions of this model, we set $\Theta=0°$ in Eq. (28) and compute R_{14} $Ga^{69}As$ to be 0.4×10^{10} cm^{-1} and R_{14} $GaAs^{75}$ to be 0.5×10^{10} cm^{-1}. Therefore, this model with the computed values of the mean-square field gradients and impurity concentrations equal to the carrier concentrations gives agreement within a factor of 3 with the previous static values[26] of R_{14}.

The results of a similar computation for the values of R_{14} for $InSb^{121}$ in the three InSb samples are shown in Table XIV. We see that the intrinsic concentration sample, InSb(1), has a value of R_{14} larger than for the other two InSb samples. It is possible that for the intrinsic samples some degree of impurity compensation takes place so that the actual ionized impurity concentration is larger than the charge carrier concentration

TABLE XIV. Values of R_{14} computed from measured mean-square field gradients and measured carrier concentrations.

Nucleus	R_{14} (10^{10} cm^{-1})
$In^{115}As$	0.7
$InAs^{75}$	0.3
$InSb^{121}(1)$	9.0
$In^{115}Sb(2)$	1.0
$InSb^{121}(2)$	1.0
$InSb^{121}(3)$	0.5
$Ga^{69}As$	0.4
$GaAs^{75}$	0.5
$Ga^{69}Sb$	0.1
$GaSb^{121}$	0.3
$AlSb^{121}$	0.7

TABLE XV. Antishielding constants, $1-\gamma_\infty$, computed from root-mean-square field gradients. For Sb, $1-\gamma_\infty$ is taken equal to 1.00 and other values of $1-\gamma_\infty$ are computed relative to that of Sb.

Nucleus	$(1-\gamma_\infty)$
Sb	1.00
In	0.92
As	0.41
Ga	0.36

measured. In Table XIV, we give results of application of the above model for R_{14} at the nuclear positions in each of the compounds except at $Al^{27}Sb$. We estimate these values are within an order of magnitude of the correct values.

The explanation of electric field gradients arising from the electric fields of the ionized substitutional impurities appears consistent with this linewidth study from the points of view of angular dependence and magnitude. It is likely that the electric fields produce increased electronic polarization of the chemical bonds. The measured field gradients can then be expected to be due to charge effects. The distribution of field gradients should be identical at the A and B nuclear positions in the same compound. Therefore, the ratio of the measured field gradients in the same compound at A and B nuclear positions should be equal to the ratio of antishielding constants[9] at the same nuclear positions. We assume that the antishielding constant is approximately equal at the same nuclear position in different compounds. Since there are common nuclear-spin systems in the compounds of Table VII, we can determine the values of the antishielding constants for In, Sb, As, and Ga relative to each other. In Table XV, we list the values of these antishielding constants, where the value for Sb is taken as 1.0. We compare the ratios of antishielding factors from Table XV and the ratios of the magnitudes of antishielding factors found previously[16] from the separated ionic contributions to the S-tensor components. There is agreement for the Ga/Sb and As/Sb ratios and approximate agreement for the In/Sb ratios.

V. SUMMARY

(1) Nuclear acoustic resonance and NMR applied to the same nuclear-spin system simplifies the identification of the linewidth broadening mechanisms. In particular, study of NAR 1 and NAR 2 second moments due to exchange allows the evaluation of both like-spin and unlike-spin exchange constants if the exchange constant dependence on interaction distance is known. Linewidths observed by NAR 1 are much more sensitive to quadrupole broadening than linewidths observed by NMR. There are two reasons:

(a) The largest transition probabilities between quadrupole split energy levels are associated with the energy values with the largest values of $|m|$.

(b) The transitions between energy levels of largest values of $|m|$ have second moments due to like-spin exchange and like-spin dipole-dipole interactions, which are smaller than the second moment of the line shape without quadrupole broadening.

(2) We find experimental agreement with the interaction distance dependence in the exchange constant derived by Anderson. The electronic wave-function densities at A and B nuclear positions are determined using Anderson's exchange constant, an assumed effective mass equal to the free-electron mass, and the experimental exchange second moments.

(3) The broadening of the resonance line shapes of each nuclear spin-system as the magnetic field is rotated from ⟨001⟩ directions is explained as due to anisotropic dipole-dipole and anisotropic quadrupole interactions. The quadrupole second moments are due to a distribution of field gradients, which are characterized by a root-mean-square field gradient. The experimental quadrupole second-moment anisotropy and the magnitude of the mean-square field gradient agree with an explanation that the electric field gradients are due to the electric fields of the ionized impurities. The tensor component R_{14} is estimated at the nuclear positions, and the ratios of the antishielding factors between In, Sb, Ga, and As nuclear positions are determined.

ACKNOWLEDGMENTS

We thank Dr. Robert A. Ruehrwein of the Monsanto Chemical Company for supplying the InAs, InSb, GaAs, and GaSb single crystals. We also thank Professor D. I. Bolef for comments regarding the manuscript.

PHYSICAL REVIEW VOLUME 185, NUMBER 2 10 SEPTEMBER 1969

Relaxation Effects in Antiferromagnetic Ferrous Carbonate†

HANG NAM OK*
Solid State and Materials Laboratory, Princeton University, Princeton, New Jersey 08540
(Received 20 March 1969)

Mössbauer studies of antiferromagnetic $FeCO_3$ below and above the Néel temperature show an asymmetric line broadening, and a constant value of 184 kOe of the magnetic hyperfine field from 0 to $\frac{1}{2}T_N$. These phenomena are explained using an Ising model with slow electron relaxation. The relaxation rate decreases with decreasing temperature, suggesting a spin-lattice relaxation. The Néel temperature was found to be (38.3±0.3)°K, which is 3.3°K higher than that measured by neutron diffraction.

INTRODUCTION

RECENTLY, electron-spin relaxation phenomena have been observed by many investigators[1–8] using Mössbauer technique. However, most of these studies in iron compounds were restricted to the Fe^{3+} ions, and to my knowledge no relaxation effects in the Fe^{2+} ions in an antiferromagnetic material have been observed. The purpose of this paper is to present the Mössbauer spectra of antiferromagnetic $FeCO_3$ at low temperatures, and to explain the observed phenomena in terms of slow electron relaxation between two lowest states of the Fe^{2+} ions.

Ferrous carbonate, occurring naturally as the mineral siderite, has a rhombohedral (calcite) structure[9] with a bimolecular unit cell which has the dimensions $a_0=5.795$ Å, $\alpha=47°45'$. Its structure may be visualized as an NaCl-type lattice contracted along a body diagonal, and, therefore, we may expect the ferrous ion to be under the influence of a crystalline electric field of cubic symmetry in the first approximation, and of the trigonal field in the second approximation. Magnetic susceptibility[10–12] and neutron diffraction[13] measurements have established antiferromagnetic behavior at low temperatures with the Fe^{2+} spins pointing along the trigonal c axis, in alternating (0 0 0 1) ferromagnetic

† Work supported by National Institutes of Health Grant No. PHS-DE 02492-02.
* Present address: Department of Physics, Yonsei University, Seoul, Korea.
[1] C. E. Johnson, T. E. Cranshaw, and M. S. Ridout, in *Proceedings of the International Conference on Magnetism, Nottingham, 1964* (The Institute of Physics and the Physical Society, London, 1965), p. 459.
[2] G. K. Wertheim and J. P. Remeika, Phys. Letters **10**, 14 (1964).
[3] M. Blume, Phys. Rev. Letters **14**, 96 (1965); M. Blume and J. A. Tjon, Phys. Rev. **165**, 446 (1968).
[4] F. E. Obenshain, L. D. Roberts, C. F. Coleman, D. W. Forester, and J. O. Thompson, Phys. Rev. Letters **14**, 365 (1965).
[5] F. van der Woude and A. J. Dekker, Phys. Status Solidi **9**, 977 (1965).
[6] H. H. Wickman, M. P. Klein, and D. A. Shirley, Phys. Rev. **152**, 345 (1966).
[7] E. Bradford and W. Marshall, Proc. Phys. Soc. (London) **87**, 731 (1966).
[8] L. E. Campbell and S. DeBenedetti, Phys. Rev. **167**, 556 (1968).
[9] R. W. G. Wyckoff, *Crystal Structures* (Wiley-Interscience, Inc., New York, 1964), Vol. 2.
[10] M. Foex, Ann. Phys. (N. Y.) **16**, 174 (1921).
[11] H. Bizette, J. Phys. Radium **12**, 161 (1951).
[12] I. S. Jacobs, J. Appl. Phys. **34**, 1106 (1963).
[13] R. A. Alikhanov, Zh. Eksperim. i. Teor. Fiz. **36**, 1690 (1959) [English transl.: Soviet Phys.—JETP **9**, 1204 (1959)].